# Spin character of interlayer excitons in tungsten dichalcogenide heterostructures: GW-BSE calculations

Yaning Li, Zhihui Yan, and Shudong Wang [*]

*School of Physical Science and Technology, Inner Mongolia University, Hohhot 010021, People's Republic of China*

Interlayer excitons (IXs) have become an ideal platform for studying exciton condensation, single-photon emission, and other quantum phenomena. Two-dimensional transition metal dichalcogenide (TMD) heterostructures, with type-II band alignment features, provide a simple framework for the formation of IXs. The intrinsic electric field of Janus TMDs can be introduced to tune the type-II band energies. In this paper, we perform GW-BSE calculations to explore how the Janus layers affect the interlayer excitations in $WSSe/WS_2$-based heterostructures by tuning the spin states. Our results reveal that the parallel-arranged intrinsic electric field structure with the S/Se interface mixes more spin-singlet state into the spin-triplet states, and hence, the lowest IX has a shorter radiative lifetime than other Janus $WSSe@WS_2$ heterostructures. We also find the S/Se interface makes the energy band more staggered and thus has no bound bright IXs. For S/S interface heterostructures in which the electric field points away from the interface, the strong band hybridization mixes 49% spin-singlet into the spin-triplet states, and therefore, the radiative lifetime of the lowest-energy bright IX is as short as $10^{-13}$ s at 0 K. Our explorations show that strong spin-orbit coupling plays a key role in the spin-singlet-triplet mixture in Janus WSSe structures by arranging the direction of the intrinsic electric field.

## I. INTRODUCTION

Monolayer transition metal dichalcogenides (TMDs) and their heterostructures have attracted attention due to their direct band gap, large exciton binding energy [1–5], and effective interlayer energy transfer [6]. The nanometer thickness of two-dimensional (2D) materials limits the electrons in the structure within the 2D range, enhances the quantum confinement effect, and brings various physical and chemical properties to the 2D materials [7–13]. In recent years, the exploration of 2D materials has not stopped, and one of them is the construction of van der Waals (vdW) heterojunctions using different 2D materials [14]. No need to consider the lattice mismatch caused by constituent monolayers in vdW heterojunctions allows for the combination of multiple materials that meet the requirements [15]. Two-dimensional heterojunctions are an essential platform for exploring the properties of charge transfer or interlayer excitons (IXs). That is because vdW TMD heterojunctions can easily establish typical type-II band alignments, which are more conducive to the formation of IXs than most other materials [4,5,16–18]. The electrons and holes in IXs reside in different layers, which significantly increases the exciton lifetime [11,19] and generates a repulsive nonzero electric dipole moment [20–28].

Since single-layer MoSSe was synthesized [29–33], Zheng *et al.* [34] have experimentally and theoretically demonstrated that the enhanced electron-phonon interaction in MoSSe results in an exciton recombination rate ∼30% faster than that in $MoS_2$. Trivedi *et al.* [29] have successfully synthesized MoSSe/WSSe heterojunctions at room temperature through the selective epitaxial atom substitution method. These findings open an area for the study of the interaction between light and matter. The transition from $MX_2$ to MXY introduces broken mirror symmetry and an out-of-plane intrinsic dipole moment due to the different electronegativities of X and Y elements. Recently, high-performance IX devices have been experimentally verified as basic candidate devices for building IX information processing circuits [35–39].

Janus heterojunctions are composed of Janus monolayer materials, with one side having different chemical and physical properties than the other. This intrinsic electric dipole moment plays a key role in the electronic, optical, and even chemical properties of 2D Janus heterojunctions. Authors of recent studies have shown that the built-in dipole field can be used to separate carriers and thus extend their recombination lifetimes [40]. Likewise, it has been found experimentally [41] that, in Janus vdW heterojunctions, the charge transfer from Janus to regular TMD single layer strongly depends on the direction of the charge current relative to the Janus field direction. These results suggest that Janus TMDs can serve as a platform for controlling oriented charge transfer characteristics in 2D heterostructures.

Based on the successful fabrication of regular@Janus TMD heterostructures [29,41,42], herein, we investigate the exciton-related optoelectronic properties of heterojunctions composed of WSSe and/or $WS_2$ monolayers, using first-principles and many-body perturbation theory. We demonstrate that the intrinsic dipole moment plays a key role in tuning the radiative lifetimes of IXs, through mixing the spin-allowed and spin-forbidden states with different stacking sequences.

[*]sdwang@imu.edu.cn

045422-1

## II. THEORIES AND METHODS

The ground-state properties are calculated using the QUAN-TUM ESPRESSO package [43,44]. Perdew-Burke-Ernzerhof functionals and optimized norm-conserving pseudopotentials are used [45], and the full relativistic effects are considered when describing spin-orbit coupling (SOC). The vdW correction is considered using the DFT-D3 scheme, with a plane-wave cutoff energy of 70 Ry. The vacuum layer is set to 20 Å to prevent interactions in the nonperiodic direction. A $41 \times 41 \times 1$ $k$-point grid is chosen to ensure convergence of the results to 100 meV. The quasiparticle energy is calculated using the $G_0W_0$ approximation, with a response function of 15 Ry. Convergence of the $G_0W_0$ band gap is achieved by using 300 empty bands plus an extrapolar correction scheme [46]. The optical absorption spectrum of the system is obtained by solving the Bethe-Salpeter equation. Since we focus on low-energy excitons, only four valence bands (VBs) and four conduction bands (CBs) are considered. The excited states properties are calculated using the YAMBO code [47,48]. The convergence tests are shown in Figs. S1 and S2 in the Supplemental Material [49].

The calculation of the radiative exciton lifetime is done using the Fermi golden rule [50,51]. At 0 K, the exciton lifetime is obtained by

$$\tau_S(0) = \gamma_S(0)^{-1} = \frac{\hbar^2 cA}{8\pi e^2 E_S(0)\mu_S^2}, \quad (1)$$

where $\hbar$ is the reduced Planck constant, $c$ is the speed of light, $E_S(0)$ is the exciton excitation energy, $A$ is the area of the unit cell, and $\mu_S$ is the transition dipole moment of the exciton. At nonzero temperature, the exciton lifetime is obtained by

$$\langle \tau_S \rangle(T) = \gamma_S(0)^{-1} \frac{3}{4} \left[ \frac{2M_S c^2 k_B T}{E_S(0)^2} \right], \quad (2)$$

where $k_B$ is the Boltzmann constant, and $M_S$ is the effective mass of the exciton, which is the sum of the effective masses of the corresponding electron and hole in the quasiparticle band energies.

## III. RESULTS AND DISCUSSION

The four AB vertical stacking configurations of Janus heterostructures of WSSe and/or WS$_2$ considered here are shown in Fig. 1. The calculated phonon spectra (Fig. S3 in the Supplemental Material [49]) indicate that all the structures herein are dynamically stable. We classify the four stacking configurations as WSSe-WSSe (1-SeS), WS$_2$-WSeS (2-SSe), WS$_2$-WSSe (3-SS), and WS$_2$-WS$_2$ (4-SS). For 1-SeS, both monolayer constituent WSSe's share the same orientations of the out-of-plane intrinsic electric field, pointing from the Se to the S atom. For 2-SSe and 3-SS, the electric field direction points toward and away from the interface, respectively. There is no electric field in 4-SS due to the homogeneity of chalcogen. Clearly, 1-SeS and 2-SSe possess the S/Se interface, whereas 3-SS and 4-SS have the S/S interface. The different interface results in the interlayer distance between the neighboring S/Se and S/S atoms being 3.21, 3.19, 3.14, and 3.16 Å for the four configurations 1-SeS, 2-SSe, 3-SS, and 4-SS, respectively. The distance is defined by the magnitude
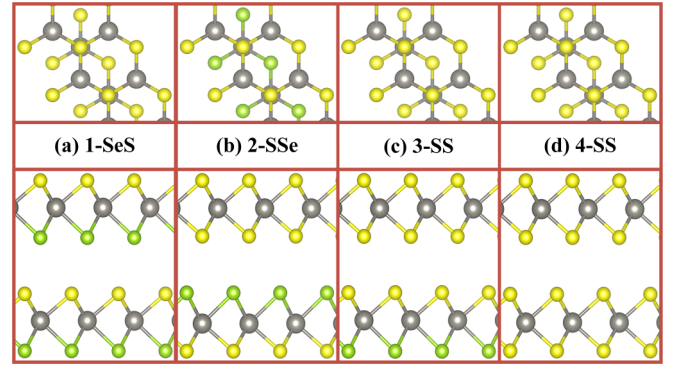


FIG. 1. Top and side views of four stacking configurations of Janus heterostructures of WSSe and/or WS$_2$. (a) WSSe@WSSe (1-SeS), (b) WS$_2$@WSeS (2-SSe), (c) WS$_2$@WSSe (3-SS), and (d) WS$_2$@WS$_2$ (4-SS). S/Se atoms are represented here by yellow/green balls.

and electronegativity of atoms S and Se in the adjacent layers. Additionally, the S/S interface exhibits stronger interlayer coupling than the S/Se interface, as demonstrated by the low-frequency Raman spectra [52].

The spin-resolved quasiparticle band structures, including the SOC of the four structures, are displayed in Fig. 2. Since we focus on the low-energy direct transitions, only the band structures in the vicinity of the $K$ point are presented here. The calculated $G_0W_0$ band gap at the $K$ point of the four structures is 1.89, 1.87, 2.47, and 2.55 eV, respectively. Additionally, as shown in the insets, all four structures have type-II band alignment, which is advantageous for producing IXs. As seen in Fig. 2, the 1-SeS and 2-SSe band structures are staggered, while the band structures of 3-SS and 4-SS are extensively overlapped because of the unique S/Se and S/S interfaces. The S/Se and S/S interfaces introduce different electrostatic potential drops $\Delta V$ between the two constituent monolayers and further alter the band alignments. We classify the band states as $|VB(CB) \pm i, U(L), \uparrow(\downarrow)\rangle$, where $i$ is the band index counted from the band edge, U(L) is the charge distribution of the band state in the upper (lower) layer, and $\uparrow(\downarrow)$ means spin-up (down) projected in the direction of the
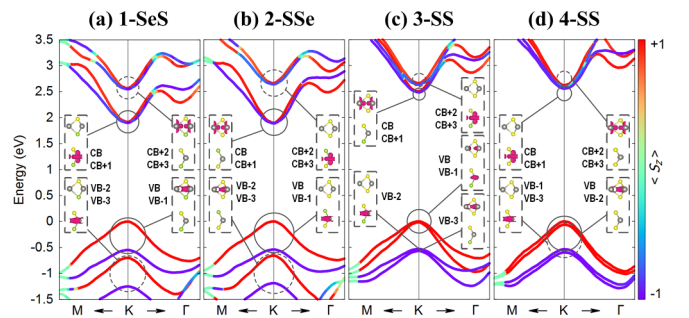


FIG. 2. Spin-resolved quasiparticle band structures of the four heterostructures around the $K$ point. The insets show the charge distributions of the top four valence (VB to VB$-3$) and bottom four (CB to CB$+3$) conduction bands at the $K$ point. The energy of the top VB at the $K$ point is set to zero. The spin-up (down) is denoted by the red (violet) color projected along the $z$ axis.
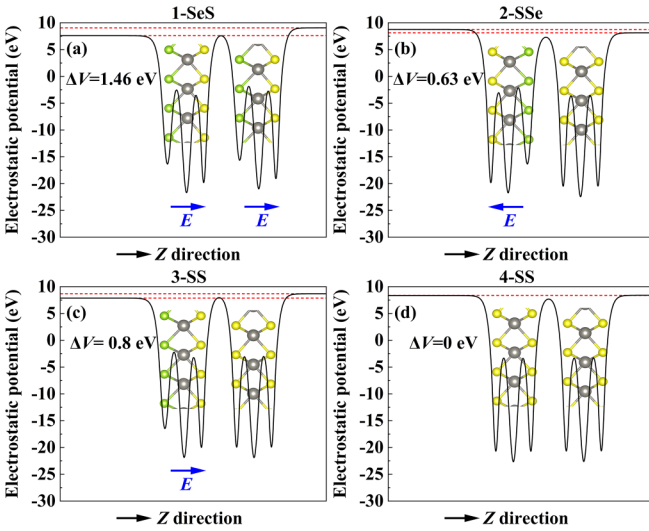
FIG. 3. The planar averaged electrostatic potentials. The intrinsic electric field within the WSSe monolayer is indicated as **E**. The $Z$ direction points from the lower to the upper layer.
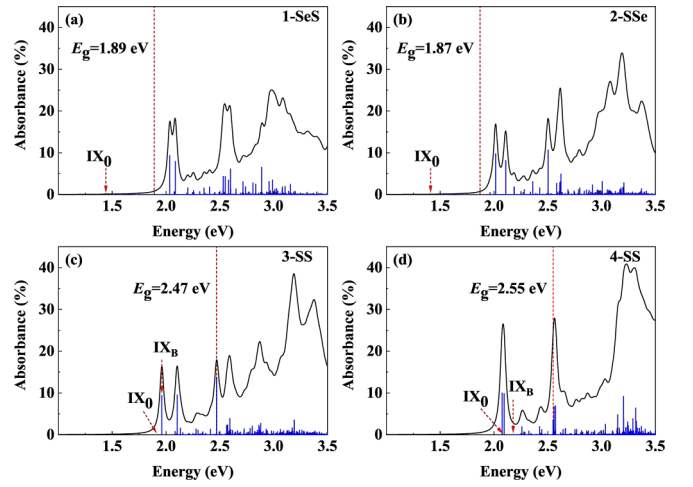


FIG. 4. Optical absorption spectra. The lowest-energy interlayer exciton (IX) is indicated as $IX_0$ and the lowest-energy bright IX is $IX_B$. The vertical solid (blue) lines are the oscillator strengths, and the dashed (red) lines represent the quasiparticle energy gap at the $K$ point.

$z$ axis. For 1-SeS, both VB ($|$VB, U, $\uparrow\rangle$) and VB-1 ($|$VB-1, U, $\downarrow\rangle$) are contributed by the upper WSSe layer with opposite spin direction. On the contrary, VB ($|$VB, L, $\uparrow\rangle$) and VB-1 ($|$VB-1, L, $\downarrow\rangle$) are from the lower WSSe layer for 2-SSe. A similar situation also occurs in the CBs. This depicts how the band sequence of 1-SeS compared with that of 2-SSe is reversed by the WS$_2$ monolayer replacement for WSSe. The 3-SS heterostructure has the same constituents as 2-SSe, but the intrinsic electric field in the WSSe monolayer is reversed with respect to 2-SSe. Here, 4-SS has similar band structures to 3-SS but with reversed VB and CB as well.

To investigate the causes of the various band structures in more detail, we computed the planar averaged electrostatic potentials of the four heterostructures as indicated in Fig. 3. The electrostatic potential drop $\Delta V$ (the potential increases along the $+z$ direction) is as large as 1.46 eV, the largest of the four structures, in the case of the 1-SeS because the out-of-plane dipole moments in both WSSe layers have the same orientation. The huge $\Delta V$ introduces a strong electric field in the out-of-plane direction and would further influence the dissociation and recombination processes of interlayer electron-hole pairs. Due to the dipole moment appearing just in the WSSe layer, 2-SSe and 3-SS have relatively small $\Delta V$, measuring 0.63 and 0.80 eV, respectively, in comparison with 1-SeS. In 2-SSe, the potential decreases in the direction of $+z$, which is opposite to 1-SeS. This opposite potential drop changing trend in the case of the S/Se interface leads to the CB and VB shifting in opposite directions, and consequently, in 1-SeS and 2-SSe, the band sequences are reversed, as shown in Fig. 2. In 3-SS, the potential increases in the direction of $+z$ as in 1-SeS but with a drop value much smaller than 1-SeS. The smaller potential drop in 3-SS is insufficient to reverse the VB and CB in contrast with 1-SeS, causing the bands from the WSSe and WS$_2$ layers to just exhibit a strong degeneracy around the $K$ point, as shown in Fig. 2(c). Here, 4-SS is a homobilayer WS$_2$ with negligible potential drop between the two constituent layers, and the incomplete band degeneracy

originates from the Davydov splitting due to the identical WS$_2$ layers [53]. The optical excitation properties, spatial distributions of the exciton wave functions, and radiative lifetimes of IXs would be strongly impacted by the varied band alignments of the four heterostructures due to the different potential drops arising from the intrinsic electric field, as indicated in the following text.

On top of the quasiparticle band structures, we compute the optical absorption properties, including the excitonic effect, as shown in Fig. 4. The lowest-energy IX is indicated as $IX_0$, and the lowest-energy bright IX is $IX_B$, both of which are doubly degenerate because of the energy degeneracy at the $K$ and $-K$ points in the Brillouin zone. According to analysis of the excitonic spin configurations in 1-SeS, we find that $IX_0$ (also the lowest-energy exciton) located at 1.44 eV with binding energy of 0.45 eV comes predominantly from the transition of $|$VB, U, $\uparrow\rangle$ to $|$CB, L, $\downarrow\rangle$ but also mixes in 5.3% of the spin-allowed transition $|$VB, U, $\uparrow\rangle$ to $|$CB+1, L, $\uparrow\rangle$. As shown in Table I, the total spin $\langle S \rangle$ is 0.964 in 1-SeS, meaning that the spin-forbidden excitation of $IX_0$, in which the $|S = 1$, $M = -1\rangle$ component accounts for 89.1%. The total spin $\langle S \rangle$ of $IX_0$ is also less than that of the other three structures, which is evidence of a strong mixture state of the singlet and triplet due to the strong SOC effect and the exchange interaction [54–56]. The radiative lifetime of $IX_0$ is if $8.43 \times 10^{-10}$ s at 0 K due to the dark characteristic (the lifetimes at 300 K are shown in Table SI in the Supplemental Material [49]).

In 2-SSe, $IX_0$ (also the lowest-energy exciton) is at 1.41 eV with the binding energy of 0.46 eV, attributed to the transition of $|$VB, L, $\uparrow\rangle$ to $|$CB, U, $\downarrow\rangle$, and primarily originates from the triplet component of $|S = 1$, $M = -1\rangle$. The total spin $\langle S \rangle$ (0.988) in the case of 2-SSe is larger than that of 1-SeS, and the triplet states account for 98.1%, indicating that the singlet-triplet mixture is weaker than in 1-SeS. The more triplet state component in 2-SSe causes a long lifetime of $IX_0$ if $8.0 \times 10^{-8}$ s at 0 K, which is two orders longer than that in 1-SeS. There are no bound bright excitons in 1-SeS or 2-SSe.

TABLE I. Excitonic spin configurations: expectation value $\langle S \rangle$ and the projections along the singlet state and along the triplet state.

|  | $\langle S \rangle$ | $|S=0, M=0\rangle$ | $|S=1, M=-1\rangle$ | $|S=1, M=0\rangle$ | $|S=1, M=1\rangle$ |
|---|---|---|---|---|---|
| 1-SeS |  |  |  |  |  |
| $IX_0$ | 0.964 | 0.053 | 0.891 | 0.053 | 0.003 |
| 2-SSe |  |  |  |  |  |
| $IX_0$ | 0.988 | 0.019 | 0.951 | 0.018 | 0.012 |
| 3-SS |  |  |  |  |  |
| $IX_0$ | 0.987 | 0.020 | 0.479 | 0.020 | 0.481 |
| $IX_B$ | 0.624 | 0.493 | 0.001 | 0.490 | 0.016 |
| 4-SS |  |  |  |  |  |
| $IX_0$ | 0.984 | 0.025 | 0.950 | 0.024 | 0.001 |
| $IX_B$ | 0.674 | 0.436 | 0.001 | 0.435 | 0.128 |

In the case of 3-SS, $IX_0$, with a binding energy of 0.55 eV, is located at 1.92 eV higher than the lowest-energy intralayer exciton. Due to the strong overlap of the VB and VB-1 at the K point, $IX_0$ here is ascribed to the mixed transitions of $|VB, U+L, \uparrow\rangle$ to $|CB, U, \downarrow\rangle$ and $|VB-1, U+L, \uparrow\rangle$ to $|CB, U, \downarrow\rangle$, which accounts for 40.8% and 58.3%, respectively. The triplet components of $|S=1, M=\pm1\rangle$ dominates the mixed transitions in 3-SS. The radiative lifetime of $IX_0$ is $1.1 \times 10^{-4}$ s at 0 K. Furthermore, we find a bright IX, $IX_B$, at 1.96 eV with a binding energy of 0.51 eV. The spin-allowed mixed transitions of $|VB, U+L, \uparrow\rangle$ to $|CB+1, U, \uparrow\rangle$ and $|VB-1, U+L, \uparrow\rangle$ to $|CB+1, U, \uparrow\rangle$, which accounts for 44.8% and 52.7%, respectively, dominate this excitation. Clearly, the total spin $\langle S \rangle$ of $IX_B$ is $\ll 1$, and the linear combination of $|S=0, M=0\rangle$ (49.3%) and $|S=1, M=0\rangle$ (49%) governs this process because of the strong SOC effect. At 0 K, the lifetime of $IX_B$ is as short as $5.39 \times 10^{-13}$ s.

In 4-SS, $IX_0$ is located at 2.09 eV with a radiative lifetime $3.21 \times 10^{-10}$ s, higher than the lowest-energy intralayer exciton as well. The singlet component accounts for 2.5%, which is greater than that of 2-SSe and 3-SS but less than half of 1-SeS. One of the factors contributing to the shorter lifetime of $IX_0$ than that of 2-SSe and 3-SS and $IX_0$ being comparable with that of 1-SeS is the substantial singlet component in 4-SS. The lowest-energy bright exciton $IX_B$ is at 2.18 eV, originating from the transitions of $|VB, U, \uparrow\rangle$ to $|CB+1, L, \uparrow\rangle$ and $|VB-1, U, \uparrow\rangle$ to $|CB+1, L, \uparrow\rangle$, which account for 88.5 and 10.6%, respectively. The lifetime of $1.02 \times 10^{-10}$ s here for $IX_B$ is three orders longer than that of 3-SS, which can be ascribed to the different dipole transition matrix elements according to the dipole selection rules. For all four structures, the parallel arrangement of the dipole moments of 1-SeS remarkably alters the ratio of the singlet component, leading to the smallest total spin $\langle S \rangle$ and thus shorter lifetime of $IX_0$.

The radiative lifetime of exciton is also dependent on the distributions of exciton wave functions. We give the real-space distributions of exciton wave functions for $IX_0$ and $IX_B$ as shown in Fig. 5. The fixed hole position is determined by the band orbital character involving transitions. For 1-SeS, the hole is fixed around the W atom of the upper WSSe layer, whereas the electrons are totally distributed in the lower WSSe layer, as shown in Fig. 1(a) and the one-dimensional wave functions. The complete spatial separation of electron and hole in $IX_0$ is affected by the direction of the intrinsic electric field. The photoexcited electrons of $IX_0$ in 1-SeS transfer

from the upper to the lower layer, which is in both directions of the two WSSe constituents, consequently promoting the transitions [41]. In the case of 2-SSe and 3-SS, both holes are fixed in the lower layer. The electric field in 2-SSe points away from the interface and promotes the transition of electrons from the lower to the upper layer, the process in which the
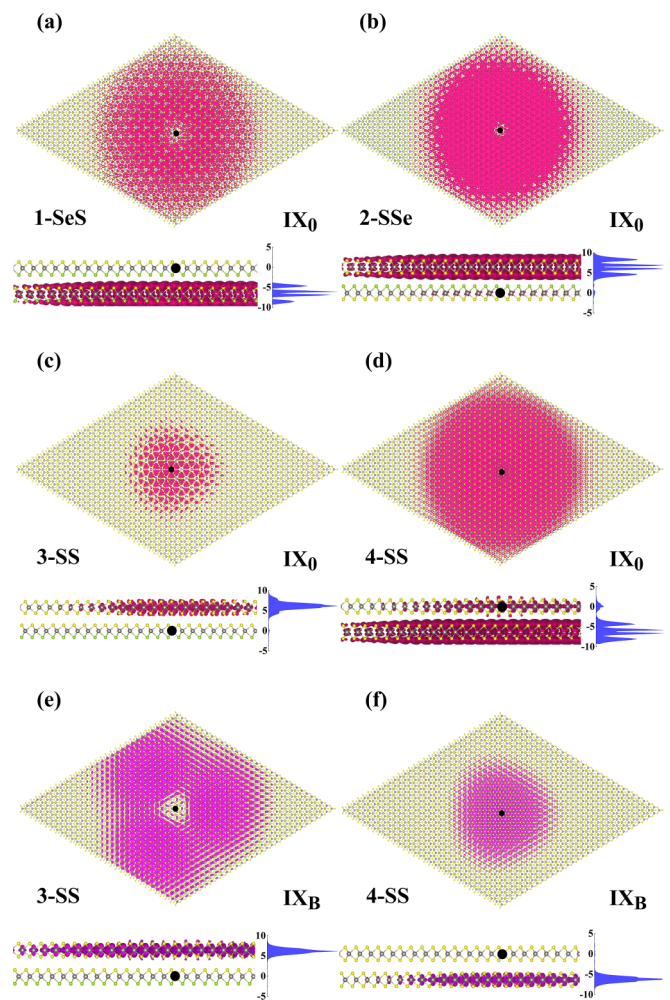


FIG. 5. Top and side views of exciton wave functions for $IX_0$ and $IX_B$. The black dots indicate the hole positions, and the insets in the side views (blue on line) are the one-dimensional exciton wave functions in the out-of-plane direction.

potential of the electrons is decreased, as shown in Fig. 3(b). For 3-SS, the electric field prevents a similar process due to the opposite electric field direction. Moreover, 2-SSe has a significant overlap between electron and hole wave functions for $IX_0$, whereas in 3-SS, the electron is well confined in the upper layer. Therefore, the very different lifetimes of $IX_0$ for both spin-forbidden excitations in 2-SSe and 3-SS appear [according to Eq. (1), the radiative lifetime is inversely proportional to the excitation energy $E_s$, but here, the $IX_0$'s we considered have the same order of magnitude as $E_s$, so we neglect this factor]. In 4-SS, $IX_0$ is a hybrid exciton in which the electron wave function extends both in the upper (11.7%) and lower (88.3%) layers. The strong overlap of electron and hole wave functions, together with the smaller S/S distance, gives rise to $IX_0$ having a lifetime comparable with that of 1-SeS.

Finally, we discuss the dipole selection rules for the four structures. The VB and CB are mainly contributed by the orbitals of $d_{xy} + d_{x^2-y^2}$ and $d_{z^2}$ of the W atoms (Table SII in the Supplemental Material [49]), and for all the structures, the point group of the bands at the $K$ point is $C_3$. According to the corresponding character table, the irreducible representations of $W - d_{z^2}$ is $A$, while other $d$ orbitals are $E$, and both the in-plane $x$- and $y$-axis transforms are $E$. According to the dipole selection rules, $W(d_{xy} + d_{x^2-y^2}) \rightarrow W(d_{z^2}) \Rightarrow E \otimes A \otimes E = 2A + E$, implying that all the VB to CB transitions satisfy the dipole selection rule. As a result, the darkness of the lowest-energy $IX_0$'s in the four structures is dominated by the spin-forbidden process.

In summary, we have investigated the interlayer excitations of the Janus WSSe structures using the GW/BSE method. Our results reveal that the intrinsic electric field strongly alters the quasiparticle band structures and the exciton states. For the heterostructures with S/Se interfaces, there are no bound bright IXs, whereas for the heterostructures with S/S interfaces, we find both dark and bright IXs. Moreover, 1-SeS with the parallel electric field mixes more spin-singlet states into the spin-triplet states than the other three structures and thus has a relatively short radiative lifetime of $IX_0$. Due to the strong hybridization, the 3-SS structure has a bright $IX_B$ with the radiative lifetime as short as $5.39 \times 10^{-13}$ s at 0 K. Our findings suggest that the direction of the electric field in the monolayer Janus structure can be used to tune the lifetime of the IX in the heterostructures.

[1] M. Q. Zhu, Z. N. Zhang, T. Zhang, D. D. Liu, H. Zhang, Z. X. Zhang, Z. L. Li, Y. C. Cheng, and W. Huang, Exchange between interlayer and intralayer exciton in $WS_2/WS_2$ heterostructure by interlayer coupling engineering, Nano Lett. **22**, 4528 (2022).

[2] Y. Kim and J. Kim, Near-field optical imaging and spectroscopy of 2D-TMDs, Nanophotonics **10**, 3397 (2021).

[3] X. L. Ma, S. H. Fu, J. W. Ding, M. Liu, A. Bian, F. Hong, J. T. Sun, X. X. Zhang, X. H. Yu, and D. W. He, Robust interlayer exciton in $WS_2/MoSe_2$ van der Waals heterostructure under high pressure, Nano Lett. **21**, 8035 (2021).

[4] R. T. Pang and S. D. Wang, Dipole moment and pressure dependent interlayer excitons in MoSSe/WSSe heterostructures, Nanoscale **14**, 3416 (2022).

[5] X. Zhang, R. T. Pang, X. R. Hou, and S. D. Wang, Stacking-tailoring quasiparticle energies and interlayer excitons in bilayer Janus MoSSe, New J. Phys. **23**, 013003 (2021).

[6] D. Kozawa, A. Carvalho, I. Verzhbitskiy, F. Giustiniano, Y. Miyauchi, S. Mouri, A. H. C. Neto, K. Matsuda, and G. Eda, Evidence for fast interlayer energy transfer in $MoSe_2/WS_2$ heterostructures, Nano Lett. **16**, 4087 (2016).

[7] D. Xiao, G. B. Liu, W. X. Feng, X. D. Xu, and W. Yao, Coupled spin and valley physics in monolayers of $MoS_2$ and other group-VI dichalcogenides, Phys. Rev. Lett. **108**, 196802 (2012).

[8] A. Splendiani, L. Sun, Y. B. Zhang, T. S. Li, J. Kim, C. Y. Chim, G. Galli, and F. Wang, Emerging photoluminescence in monolayer $MoS_2$, Nano Lett. **10**, 1271 (2010).

[9] A. Chernikov, T. C. Berkelbach, H. M. Hill, A. Rigosi, Y. Li, B. Aslan, D. R. Reichman, M. S. Hybertsen, and T. F. Heinz, Exciton binding energy and nonhydrogenic rydberg series in monolayer $WS_2$, Phys. Rev. Lett. **113**, 076802 (2014).

[10] A. T. Hanbicki, K. M. McCreary, G. Kioseoglou, M. Currie, C. S. Hellberg, A. L. Friedman, and B. T. Jonker, High room temperature optical polarization due to spin-valley coupling in monolayer $WS_2$, AIP Adv. **6**, 055804 (2016).

[11] Y. L. Li, Y. Rao, K. F. Mak, Y. M. You, S. Y. Wang, C. R. Dean, and T. F. Heinz, Probing symmetry properties of few-layer $MoS_2$ and h-BN by optical second-harmonic generation, Nano Lett. **13**, 3329 (2013).

[12] N. Kumar, S. Najmaei, Q. Cui, F. Ceballos, P. M. Ajayan, J. Lou, and H. Zhao, Second harmonic microscopy of monolayer $MoS_2$, Phys. Rev. B **87**, 161403(R) (2013).

[13] L. Britnell, R. M. Ribeiro, A. Eckmann, R. Jalil, B. D. Belle, A. Mishchenko, Y. J. Kim, R. V. Gorbachev, T. Georgiou, S. V. Morozov *et al.*, Strong light-matter interactions in heterostructures of atomically thin films, Science **340**, 1311 (2013).

[14] A. K. Geim and I. V. Grigorieva, Van der Waals heterostructures, Nature (London) **499**, 419 (2013).

[15] N. P. Wilson, W. Yao, J. Shan, and X. D. Xu, Excitons and emergent quantum phenomena in stacked 2D semiconductors, Nature (London) **599**, 383 (2021).

[16] J. Palepu, P. P. Anand, P. Parshi, V. Jain, A. Tiwari, S. Bhattacharya, S. Chakraborty, and S. Kanungo, Comparative analysis of strain engineering on the electronic properties of homogenous and heterostructure bilayers of $MoX_2$ ($X$ = S, Se, Te), Micro Nano Lett. **168**, 207334 (2022).

[17] N. Peimyoo, T. Deilmann, F. Withers, J. Escolar, D. Nutting, T. Taniguchi, K. Watanabe, A. Taghizadeh, M. F. Craciun, K. S. Thygesen *et al.*, Electrical tuning of optically active interlayer excitons in bilayer $MoS_2$, Nat. Nanotechnol. **16**, 888 (2021).

[18] Y. Jiang, S. L. Chen, W. H. Zheng, B. Y. Zheng, and A. L. Pan, Interlayer exciton formation, relaxation, and transport in TMD van der Waals heterostructures, Light Sci. Appl. **10**, 72 (2021).

[19] Q. H. Tan, A. Rasmita, S. Li, S. Liu, Z. M. Huang, Q. H. Xiong, S. A. Yang, K. S. Novoselov, and W. B. Gao, Layer-engineered interlayer excitons, Sci. Adv **7**, eabh0863 (2021).

[20] L. V. Butov, A. Zrenner, G. Abstreiter, G. Böhm, and G. Weimann, Condensation of indirect excitons in coupled AlAs/GaAs quantum wells, Phys. Rev. Lett. **73**, 304 (1994).

[21] A. A. High, E. E. Novitskaya, L. V. Butov, M. Hanson, and A. C. Gossard, Control of exciton fluxes in an excitonic integrated circuit, Science **321**, 229 (2008).

[22] W. J. Li, X. Lu, S. Dubey, L. Devenica, and A. Srivastava, Dipolar interactions between localized interlayer excitons in van der Waals heterostructures, Nat. Mater. **19**, 624 (2020).

[23] T. Fukuzawa, E. E. Mendez, and J. M. Hong, Phase transition of an exciton system in GaAs coupled quantum wells, Phys. Rev. Lett. **64**, 3066 (1990).

[24] A. T. Hanbicki, H. J. Chuang, M. R. Rosenberger, C. S. Hellberg, S. V. Sivaram, K. M. McCreary, I. I. Mazin, and B. T. Jonker, Double indirect interlayer exciton in a $MoSe_2/WSe_2$ van der Waals heterostructure, ACS Nano **12**, 4719 (2018).

[25] T. M. Wang, S. N. Miao, Z. P. Li, Y. Z. Meng, Z. G. Lu, Z. Lian, M. Blei, T. Taniguchi, K. Watanabe, S. Tongay *et al.*, Giant valley-Zeeman splitting from spin-singlet and spin-triplet interlayer excitons in $WSe_2/MoSe_2$ heterostructure, Nano Lett. **20**, 694 (2020).

[26] E. Torun, H. P. C. Miranda, A. Molina-Sanchez, and L. Wirtz, Interlayer and intralayer excitons in $MoS_2/WS_2$ and $MoSe_2/WSe_2$ heterobilayers, Phys. Rev. B **97**, 245427 (2018).

[27] P. Rivera, J. R. Schaibley, A. M. Jones, J. S. Ross, S. F. Wu, G. Aivazian, P. Klement, K. Seyler, G. Clark, N. J. Ghimire *et al.*, Observation of long-lived interlayer excitons in monolayer $MoSe_2$-$WSe_2$ heterostructures, Nat. Commun. **6**, 6242 (2015).

[28] M. Brotons-Gisbert, H. Baek, A. Molina-Sanchez, A. Campbell, E. Scerri, D. White, K. Watanabe, T. Taniguchi, C. Bonato, and B. D. Gerardot, Spin-layer locking of interlayer excitons trapped in moiré potentials, Nat. Mater. **19**, 630 (2020).

[29] D. B. Trivedi, G. Turgut, Y. Qin, M. Y. Sayyad, D. Hajra, M. Howell, L. Liu, S. J. Yang, N. H. Patoary, H. Li *et al.*, Room-temperature synthesis of 2D Janus crystals and their heterostructures, Adv. Mater. **32**, 2006320 (2020).

[30] A. Y. Lu, H. Y. Zhu, J. Xiao, C. P. Chuu, Y. M. Han, M. H. Chiu, C. C. Cheng, C. W. Yang, K. H. Wei, Y. M. Yang *et al.*, Janus monolayers of transition metal dichalcogenides, Nat. Nanotechnol. **12**, 744 (2017).

[31] J. Zhang, S. Jia, I. Kholmanov, L. Dong, D. Q. Er, W. B. Chen, H. Guo, Z. H. Jin, V. B. Shenoy, L. Shi *et al.*, Janus monolayer transition-metal dichalcogenides, ACS Nano **11**, 8192 (2017).

[32] Y. C. Lin, C. Z. Liu, Y. L. Yu, E. Zarkadoula, M. Yoon, A. A. Puretzky, L. B. Liang, X. R. Kong, Y. Y. Gu, A. Strasser *et al.*, Low energy implantation into transition-metal dichalcogenide monolayers to form Janus structures, ACS Nano **14**, 3896 (2020).

[33] M. M. Petric, M. Kremser, M. Barbone, Y. Qin, Y. Sayyad, Y. X. Shen, S. Tongay, J. J. Finley, A. R. Botello-Mendez, and K. Muller, Raman spectrum of Janus transition metal dichalcogenide monolayers WSSe and MoSSe, Phys. Rev. B **103**, 035414 (2021).

[34] T. Zheng, Y. C. Lin, Y. L. Yu, P. Valencia-Acuna, A. A. Puretzky, R. Torsi, C. Z. Liu, I. N. Ivanov, G. Duscher, D. B. Geohegan *et al.*, Excitonic dynamics in Janus MoSSe and WSSe monolayers, Nano Lett. **21**, 931 (2021).

[35] Y. D. Liu, H. L. Fang, A. Rasmita, Y. Zhou, J. T. Li, T. Yu, Q. H. Xiong, N. Zheludev, J. Liu, and W. B. Gao, Room temperature nanocavity laser with interlayer excitons in 2D heterostructures, Sci. Adv. **5**, eaav4506 (2019).

[36] T. V. Vu, H. V. Phuc, S. Ahmad, V. Q. Nha, C. V. Lanh, D. P. Rai, A. I. Kartamyshev, K. D. Pham, L. C. Nhan, and N. N. Hieu, Outstanding elastic, electronic, transport and optical properties of a novel layered material $C_4F_2$: First-principles study, RSC Adv. **11**, 23280 (2021).

[37] E. Y. Paik, L. Zhang, G. W. Burg, R. Gogna, E. Tutuc, and H. Deng, Interlayer exciton laser of extended spatial coherence in atomically thin heterostructures, Nature (London) **576**, 80 (2019).

[38] G. Grosso, J. Graves, A. T. Hammack, A. A. High, L. V. Butov, M. Hanson, and A. C. Gossard, Excitonic switches operating at around 100 K, Nat. Photon. **3**, 577 (2009).

[39] J. Kang, S. Tongay, J. Zhou, J. B. Li, and J. Q. Wu, Band offsets and heterostructures of two-dimensional semiconductors, Appl. Phys. Lett. **102**, 012111 (2013).

[40] X. C. Ma, X. Wu, H. D. Wang, and Y. C. Wang, A Janus MoSSe monolayer: A potential wide solar-spectrum water-splitting photocatalyst with a low carrier recombination rate, J. Mater. Chem. A **6**, 2295 (2018).

[41] T. Zheng, Y. C. Lin, N. Rafizadeh, D. B. Geohegan, Z. H. Ni, K. Xiao, and H. Zhao, Janus monolayers for ultrafast and directional charge transfer in transition metal dichalcogenide heterostructures, ACS Nano **16**, 4197 (2022).

[42] U. Erkılıç, S. Wang, Y. Sekine, and Y. Taniyasu, Stacking-order-dependent interlayer coupling in Janus WSSe/$WS_2$ heterostructures, Appl. Phys. Lett. **121**, 113102 (2022).

[43] P. Giannozzi, O. Andreussi, T. Brumme, O. Bunau, M. B. Nardelli, M. Calandra, R. Car, C. Cavazzoni, D. Ceresoli, M. Cococcioni *et al.*, Advanced capabilities for materials modelling with QUANTUM ESPRESSO, J. Phys. Condens. Matter **29**, 465901 (2017).

[44] P. Giannozzi, S. Baroni, N. Bonini, M. Calandra, R. Car, C. Cavazzoni, D. Ceresoli, G. L. Chiarotti, M. Cococcioni, I. Dabo *et al.*, QUANTUM ESPRESSO: A modular and open-source software project for quantum simulations of materials, J. Phys. Condens. Matter **21**, 395502 (2009).

[45] D. R. Hamann, Optimized norm-conserving Vanderbilt pseudopotentials, Phys. Rev. B **88**, 085117 (2013).

[46] F. Bruneval and X. Gonze, Accurate GW self-energies in a plane-wave basis using only a few empty states: Towards large systems, Phys. Rev. B **78**, 085125 (2008).

[47] A. Marini, C. Hogan, M. Gruning, and D. Varsano, YAMBO: An *ab initio* tool for excited state calculations, Comput. Phys. Commun. **180**, 1392 (2009).

[48] D. Sangalli, A. Ferretti, H. Miranda, C. Attaccalite, I. Marri, E. Cannuccia, P. Melo, M. Marsili, F. Paleari, A. Marrazzo *et al.*, Many-body perturbation theory calculations using the YAMBO code, J. Phys. Condens. Matter **31**, 325902 (2019).

[49] See Supplemental Material at http://link.aps.org/supplemental/10.1103/PhysRevB.109.045422 for the convergence tests, phonon spectra, exciton radiative lifetimes, and orbitals of VBs and CBs involving the transitions.

[50] H. Y. Chen, V. A. Jhalani, M. Palummo, and M. Bernardi, *Ab initio* calculations of exciton radiative lifetimes in bulk crystals, nanostructures, and molecules, Phys. Rev. B **100**, 075135 (2019).

[51] M. Palummo, M. Bernardi, and J. C. Grossman, Exciton radiative lifetimes in two-dimensional transition metal dichalcogenides, Nano Lett. **15**, 2794 (2015).

[52] K. Y. Zhang, Y. F. Guo, D. T. Larson, Z. Y. Zhu, S. A. Fang, E. Kaxiras, J. Kong, and S. X. Huang, Spectroscopic signatures of interlayer coupling in Janus MoSSe/MoS$_2$ heterostructures, ACS Nano **15**, 14394 (2021).

[53] F. Paleari, T. Galvani, H. Amara, F. Ducastelle, A. Molina-Sanchez, and L. Wirtz, Excitons in few-layer hexagonal boron nitride: Davydov splitting and surface localization, 2D Mater. **5**, 045017 (2018).

[54] M. Rohlfing and S. G. Louie, Electron-hole excitations and optical spectra from first principles, Phys. Rev. B **62**, 4927 (2000).

[55] L. Guo, M. Wu, T. Cao, D. M. Monahan, Y. H. Lee, S. G. Louie, and G. R. Fleming, Exchange-driven intravalley mixing of excitons in monolayer transition metal dichalcogenides, Nat. Phys. **15**, 228 (2019).

[56] M. Marsili, A. Molina-Sanchez, M. Palummo, D. Sangalli, and A. Marini, Spinorial formulation of the GW-BSE equations and spin properties of excitons in two-dimensional transition metal dichalcogenides, Phys. Rev. B **103**, 155152 (2021).